Open access • Journal Article • DOI:10.1038/S41565-018-0163-6

Single-layer graphene modulates neuronal communication and augments membrane ion currents — Source link

Niccolò Paolo Pampaloni, Martin Lottner, Michele Giugliano, Michele Giugliano ...+8 more authors

Institutions: International School for Advanced Studies, Technische Universität München, MIND Institute, University of Sheffield ...+4 more institutions

Published on: 11 Jun 2018 - Nature Nanotechnology (Nature Publishing Group)

Single-layer graphene modulates neuronal communication and augments membrane ion currents

Single-layer graphene modulates neuronal communication and augments membrane ion currents

Niccolò Paolo Pampaloni[1a], Martin Lottner[2a], Michele Giugliano[3,4,5], Alessia Matruglio[6b], Francesco D'Amico[7], Maurizio Prato[8,9,10], Josè Antonio Garrido[11,12*], Laura Ballerini[1*], Denis Scaini[1,7*]

[1] International School for Advanced Studies (SISSA), Trieste, Italy
[2] Walter Schottky Institut and Physik-Department, Technische Universität München, Am Coulombwall, Garching, Germany
[3] Molecular, Cellular, and Network Excitability, Department of Biomedical Sciences, Universiteit Antwerpen, Antwerpen, Belgium
[4] Department of Computer Science, University of Sheffield, S1 4DP Sheffield, UK
[5] Lab of Neural Microcircuitry, Brain Mind Institute, EPFL, CH-1015 Lausanne, Switzerland
[6] CNR-IOM - Istituto Officina dei Materiali, Area Science Park – Basovizza, S.S. 14 km 163,5 Trieste - Italy
[7] Elettra Sincrotrone Trieste S.C.p.A., S.S. 14 Km 163.5 in Area Science Park, I-34149 Trieste, Italy
[8]Department of Chemical and Pharmaceutical Sciences, University of Trieste, Trieste, Italy
[9]Nanobiotechnology Laboratory, CIC biomaGUNE, San Sebastiàn, Spain
[10]Ikerbasque, Basque Foundation for Science, Bilbao, Spain
[11]Catalan Institute of Nanoscience and Nanotechnology (ICN2), CSIC and The Barcelona Institute of Science and Technology, Campus UAB, Bellaterra, 08193 Barcelona, Spain
[12]ICREA, Pg. Lluís Companys 23, 08010 Barcelona, Spain

[a] these authors equally contributed to the work
[b] Present address: CERIC-ERIC (Central European Research Infrastructure Consortium), Area Science Park, Basovizza, S.S. 14 km 163,5 Trieste, Italy

Abstract

The use of graphene-based materials to engineer sophisticated bio-sensing interfaces adaptable to the central nervous system, requires a detailed comprehension of the behaviour of such materials in a biological context. Graphene peculiar properties may cause various cellular changes, but the underlying mechanisms remain unclear. Here, we show that single-layer graphene increases neuronal firing *via* altering membrane-associated functions in cultured cells. Graphene tunes the extracellular ions distribution at the interface with neurons, a key regulator of neuronal excitability. The resulting membrane biophysical changes include stronger potassium ion currents, with a significant shift in the fraction of neuronal firing phenotypes from *adapting* to *tonically firing*. By experimental and theoretical approaches we hypothesize that crucial to these effects are the graphene-ion interactions that are maximized when single layer graphene is deposited on electrically insulating substrates.

Graphene is a highly versatile two-dimensional nanomaterial widely adopted in many domains of science and technology, including advanced biomedical applications, due to its important physical properties [1,2,3]. Its high carrier mobility and optical transparency enable, for example, the design of novel transparent electrodes in optoelectronics [4]. Combining these features and, in particular, its remarkable electro-conductivity, makes graphene extremely appealing in neuroengineering, with reference to invasive implant technologies for brain biosensors and electrodes [5,6,7]. Despite the great interest and hopes raised by late development in graphene applications, the understanding of its functional interactions with the brain tissue is

still limited, particularly concerning the close proximity of a single plain layer of carbon atoms and the neuronal membrane ion fluxes in a biological milieu. So far, reports have shown that graphene-based materials can be safely interfaced with active neuronal cells [8,9,10], however an in-depth study on the influence of single-layer graphene (SLG) on the biophysics of neurons and *ex vivo* neuronal microcircuits upon is missing. In numerous electroceuticals applications [11,12], graphene is in contact with the extracellular environment that surrounds the excitable cell membranes. We thus asked: can SLG directly or indirectly alter neuronal activity? Which manipulations of graphene might be adopted to regulate *ad hoc* these interactions? Answering to these questions appears pivotal for future research in bio-hybrid electronic devices and, more in general, for providing insights on the deep interactions of technology with nature. Here, SLG obtained by chemical vapour deposition (CVD) was used to interface mammalian neurons, dissociated from the rat hippocampi, as a culture substrate. We employed different architectures of a single-atomic layer graphene: (i) in contact with electrically-insulating/conductive substrates or (ii) suspended. By these arrangements, we studied the collective electrical activity of neuronal networks coupled on graphene and demonstrated that, when suspended, SLG increased neuronal excitability *via* inducing specific changes in membrane biophysics. These consist in a significant shift of the fraction of neuronal firing phenotypes from *adapting* to *tonically* firing. We then propose that graphene selectively modifies membrane-associated neuronal functions and hypothesize a specific interaction between graphene and cations, in particular potassium, in the extracellular solution crucially regulating cell excitability.

SLG potentiates cell signalling in neuronal networks

80 Large films of SLG and multi-layer graphene (MLG) were characterized by atomic
81 force microscopy (AFM) and compared to glass pristine (Control) and gold-metalized
82 (Au) glass samples (Fig. 1a). The quality of CVD-grown SLG and MLG samples was
83 assessed by Raman and X-Ray photo-electron analysis. The recorded Raman
84 spectra (Fig. 1b) supports the high quality of the SLG and MLG, by the low I_D/I_G
85 ratios indicating a small amount of sp^3 hybridized carbon atoms at grain boundaries
86 or binding surface moieties [13]. X-Ray photo-electron spectroscopy (XPS) analysis
87 reveals that both SLG and MLG samples contain a low degree of metal
88 contamination (Fig. 1c).
89 To probe the electrical behaviour of excitable biological cells, we plated hippocampal
90 neurons directly on graphene- and Au-coated coverslips. Recently, several reports
91 described the successful growth of different cell types on graphene and graphene-
92 based materials [9,14,15], but rarely investigating the *ex vivo* development and
93 functional analysis of primary mammalian cells and neuronal microcircuits on
94 uncoated monolayer of graphene. Neurons plated on glass coverslips were instead
95 used as Control cultures [16,17,18]. SLG, MLG and Au substrates allow the growth
96 of cells, with comparable mature morphology to Control (Fig. 2a). We further probed
97 neuronal networks viability by quantifying network size and the ratio between
98 neuronal and glial cells after 8-10 *days in vitro* (DIV), using immunofluorescence
99 markers for neurons (class III β-tubulin) and astrocytes (GFAP). No differences were
100 detected across all groups (Fig. 2b).
101 In culture, neurons develop functional synapses and display spontaneous collective
102 electrical activity as a result of recurrent connections. We recorded spontaneous
103 synaptic activity after 8÷10 DIV. This is indirectly informative of the combined effect
104 of existence, number, transfer gain of neuronal connections, and intensity of

105 collective neuronal interactions. Heterogeneous post-synaptic currents (PSC,
106 Supplementary Fig. 1b) were detected as inward currents of variable amplitudes [16]
107 in all conditions, as shown in Figure 2c. While PSCs amplitude recorded from
108 neurons growing on SLG, MLG and Au were similar to Control (top box plots in Fig.
109 2c) the PSCs frequency (bottom) was significantly higher in SLG than in other
110 conditions. Instead, both MLG (chemically similar to SLG), and Au (chemically
111 different but characterized by high electrical conductivity), did not affect the
112 frequency of the synaptic events. The observed effect on PSCs is independent of the
113 SLG film transfer-method used (Supplementary Fig. 1a). This suggests the
114 mechanistic involvement of specific properties of the plain sheet of carbon atoms, in
115 the modulation of PSCs frequency, but only when assembled as a monolayer.
116 Miniature synaptic currents (mPSCs; Fig. 3a) were then recorded in a subset of
117 Control and SLG neurons by further application of the fast-inactivating voltage-gated
118 sodium channel blocker, tetrodotoxin (TTX, 1 μM), which impairs the action
119 potentials (APs) and thus blocks network activity. Studying mPSCs allows
120 disambiguating dynamical from structural components of the emerging network
121 activity. In particular, mPSCs reflect the stochastic release of vesicles from the
122 presynaptic terminals at individual synapses impinging onto the recorded neuron:
123 their frequency depends on the pre-synaptic release probability and on the number
124 of synaptic contacts, while their amplitude depends on postsynaptic receptor
125 sensitivity [19]. As pointed out by the box plots in Figure 3a, we found significant
126 difference neither in the frequency nor the amplitude of mPSCs, recorded in Control
127 or SLG conditions. This suggests that the increased PSCs activity described earlier
128 in SLG does not involve structural changes in the number or properties of synaptic
129 connections. This is further supported by immune-labelling experiments, where the

130 number of VGlut1-positive *puncta*, used to label and identify glutamatergic
131 presynaptic terminals [20], was not altered by the presence of SLG (Fig. 3b).
132 To rule out that SLG could interfere with the network composition or the maturation
133 of inhibitory neurons, we carefully considered two alternative hypotheses. In the first
134 one, the fraction of excitatory to inhibitory neurons is altered by SLG (e.g. in favour of
135 the former), thus biasing the spontaneous network electrical activity detected as
136 PSCs. We thus performed co-immunostaining with antibodies anti-class III β-tubulin
137 and anti-GABA (Fig. 3c) and quantified the percentage of double-positive cells,
138 indicating exclusively inhibitory neurons. In Control and SLG, we detected a
139 comparable probability of finding double-positive cells (plot in Fig. 3c), thus ruling out
140 SLG-induced alterations in the excitatory/inhibitory balance.
141 In the second hypothesis, SLG slows down the maturation of chloride ion fluxes
142 through $GABA_A$ receptors. In neurons, the intracellular chloride concentration
143 determines the amplitude of the inhibitory currents and, across successive
144 developmental stages, shifts from higher to lower values, compared to the
145 extracellular milieu [21]. Correspondingly, the activation of $GABA_A$ receptors results
146 in a depolarizing (hyperpolarizing) drive of immature (mature) neurons [22]. We
147 performed chloride imaging in living cells, using a quinoline-based Cl^- indicator dye:
148 MQAE (N-[6-methoxyquinolyl] acetoethyl ester) [23]. As reported in Supplementary
149 Fig. 2a, SLG had no impact in the GABAergic system maturation *in vitro*, a notion
150 further supported by NKCC1 quantification (Supplementary Fig. 2b).
151 Thus, the SLG-mediated increase in neuronal signalling involve neither major
152 network synaptic rearrangements, such as increased synaptogenesis, nor alterations
153 in network composition or maturation of network inhibition.

154 To ultimately clarify the biophysical mechanisms leading to the boost in
155 neuronal activity exhibited only by SLG, we examined single-cell excitability by
156 current-clamp recordings. When Control and SLG neurons were hold at –60 mV in
157 standard extracellular solution, an unbiased comparison of the basal AP frequency
158 (Fig. 4a) could be obtained. Consistent with the PSC observations, we detected a
159 significantly higher AP frequency in SLG neurons than in Control ones.
160 The subsequent bath addition of antagonists, selective for excitatory and inhibitory
161 synaptic receptors, such as Gabazine (5 μM), CNQX (20 μM) and APV (50 μM), was
162 employed to functionally decouple the recorded neurons from the synaptic network.
163 Under these conditions, intrinsic neuronal active membrane properties were
164 evaluated evoking AP responses by positive current pulses, delivered from the same
165 resting potential (–60 mV) [24,25]. When comparing the AP overshoot amplitude,
166 half-amplitude width, threshold and maximal rising slope [25,26,27] in Control and
167 SLG conditions no significant difference was found in the two groups (see Methods).
168 All these considerations taken together suggest no major involvement of voltage-
169 gated fast-inactivating Na^+ channel [27,28,29] in explaining the SLG-induced effects.
170 In addition, at –60 mV resting potential, under the cocktail of synaptic
171 blockers, brief and sufficiently strong depolarizing pulses (2÷4 ms; 1 nA) easily
172 evoked single APs in SLG and Control. The voltage trajectory of evoked single APs
173 was followed by a transient after-hyperpolarizing (AHP) in SLG neurons, while only
174 by a small after depolarization (ADP) in Control (Fig. 4b). When quantified in terms of
175 the area below such trajectories, referred to the resting potential as baseline
176 (histogram in Fig. 4b), the AHP in SLG neurons was significantly different than the
177 ADP detected in Control. Figure 4b shows the sensitivity of the AHP to various K^+
178 channel-blockers. All these observations demonstrate that the AHP detected in SLG

179 neurons was likely mediated by mixed K^+ conductances, including those activated by
180 intracellular accumulation of free Ca^{++} [30,31]. The expression of these membrane
181 channels is functionally related to spike-frequency adaptation, where sustained APs
182 progressively slow-down over time. We then further examined the sustained
183 discharge patterns of Control and SLG neurons, by injecting longer (1 s; 200 pA)
184 depolarizing pulses (Fig. 4c and 4e). In the majority (81.8%; Fig. 4d) of Control
185 neurons, sustained AP firing was dominated by spike frequency adaptation, which
186 we named *adapting* discharge phenotype. This often resulted in an early burst of
187 closely spaced APs, followed by a progressive decay of AP amplitudes, leading to
188 adaptation. On the contrary, SLG neurons (83.3%; Fig. 4d) showed no APs
189 adaptation, which we named *tonic* discharge phenotype, where cells fired
190 continuously without apparent accommodation [32,33]. Taken together, these data
191 hint at a complex homeostasis in the K^+ currents expressed by neurons when
192 coupled to SLG substrates. This hypothesis was reinforced by results obtained under
193 voltage-clamp in control and SLG neurons, where depolarizing voltage pulses
194 starting from a –60 mV holding potential baseline evoked an outward current (Fig.
195 4f), presumably due to the activation of a mixed population of K^+ channels. When
196 examined under these conditions, SLG neurons were characterized by a significantly
197 larger outward current at positive potentials, shown in the steady-state
198 current/voltage (I/V) plot of Figure 4f, likely consequence of an up-regulation of
199 mixed K^+ currents. This evidence taken together strongly indicates that SLG
200 substrates induce active changes in the electrical properties of growing neurons,
201 presumably related to altered homeostasis of K^+ membrane currents and leading to a
202 modulation of the single-cell firing phenotypes and ultimately to an increased
203 network activity. Importantly, SLG neurons generated more APs when compared to

Controls, even in response to milder and shorter stimuli (Supplementary Fig. 3a and b).

The observed correlations between single-cell properties, resulting phenotype, and network effects were further investigated by mathematical modelling. We addressed the causality between neuronal firing patterns and network activity, by examining a spike-rate model of the electrical activity emerging in populations of cultured neurons with recurrent synaptic connections (Fig. 5a).

We simulated a network of 1600 neurons with a fraction of excitatory to inhibitory neurons equal to 80/20 [34]. Since inhibitory cells usually display a tonic electrical phenotype only, we hypothesized that the change in the ratio between adapting and tonically firing neurons observed in our experiments, occurred in excitatory cells only. We therefore modelled two subpopulations of excitatory neurons: one with *adapting* and the other with *tonic* phenotypes. We found that the higher the relative fraction of *tonic* firing neurons, the higher the rate of occurrence of synchronized bursts (Fig. 5b and 5c). This supports the conclusion that the observed increase in the frequency of spontaneous (PSCs/APs) activity (Fig. 2c, SLG) is caused by the different ratio of cells with *adapting*/*tonic* phenotypes.

The potassium ions hypothesis

By a biophysical model, we tested *in silico* two mutually non-exclusive hypotheses for the observed changes in single-cell firing phenotype: (i) an increase in the total outward ionic conductance or, alternatively, (ii) a modest depletion in the extracellular concentration of K^+ ions. The rationale behind these single-cell simulations is that either SLG induced a chronic increase in ion currents involved in firing regulation, or SLG acutely altered cell firing by changing ion mobility.

229 In our model, by stripping down cell excitability to its bare essential, we explored
230 whether stronger outward potassium currents may favour excitability. We found that
231 the progressive sodium current inactivation (Fig. 5d, lower left, green traces) –
232 occurring for simplicity in the model only over *fast* time scales – could be
233 counterbalanced by strong K^+ currents (Fig. 5d, lower right, red traces) resulting in a
234 sustained, tonic, response to an external current stimulus (i.e. compare Fig. 5d to
235 4c), instead of a progressive firing inactivation. While this effect is reversed by
236 simulating an overexpression of Na^+ channels (e.g. at the axon initial segment), it
237 serves us here as a proof of concept of a counter-intuitive phenomenon: increasing
238 outward currents increases cellular excitability, by removing sodium current
239 inactivation. Of course, an *ad hoc* increase in the maximal conductance of Na^+
240 channels also increases excitability, although – in the model – with distinct features
241 in the type of transition associated to the *limit cycle* to sustained AP firing
242 (Supplementary Fig. 4). Therefore, in the model the more K^+ channels the higher the
243 excitability, in those regimes where progressive sodium inactivation affects firing
244 (Fig. 5e).
245 Outward K^+ currents also depend on the ionic driving force beyond on the maximal
246 conductance (i.e. $I_K \sim G_K\,(E_K - V)$ - see Methods), so that a change in the local ionic
247 composition might reverse sodium inactivation too. In fact, the Nernst equilibrium
248 potential E_K depends on the K^+ concentrations outside and inside the membranes
249 [35]. Should SLG interfere extracellularly with K^+ bulk diffusion in its proximity (see
250 below) then a depletion of K^+ (e.g. 10-20%, as $[K^+]_{EX} \rightarrow \delta \cdot [K^+]_{EX},\ \delta = 0.8 - 0.9$),
251 would lead to an increase in the ionic driving force, as E_K would decrease
252 accordingly (i.e. ~2-5 mV). By simulations (Fig. 5f), we found that a modest decrease
253 in E_K (e.g. from –75 to –77.6 mV) could indeed counterbalance sodium inactivation,

254 at least for an intermediate external stimulus intensity and without altering
255 significantly the resting membrane potential.
256 We thus speculate that changes in excitability of cells coupled to SLG might be
257 caused by an extracellular reduced mobility of K^+ at the interface between the
258 nanomaterial and the solution, leading to a K^+ depletion at the neuronal membranes.
259

260 **Localized potassium ions depletion in cell-substrate cleft**

261 We hypothesize that at the core of SLG ability to alter neuronal excitability is the ion
262 adsorption on graphene surfaces. This may result in a modification of ion mobility, in
263 particular K^+, at the neuronal/graphene interface.
264 Within this proposed mechanism, it is still unclear how SLG might modify K^+ ion
265 mobility while MLG (or Au) do not. It is well known that carbon-based π electron-rich
266 surfaces show a significant surface enrichment of cations in ionic solutions, due to
267 specific cation-π interactions [36,37,38,39]. Because of its size, in solution, K^+ ions
268 are weaklier solvated by water, when compared to other species (e.g. Li^+ or Na^+
269 ions) but are still good π binders. This feature makes K^+ the best alkali metal binder
270 to carbon-based surfaces in aqueous solutions [38,39]. This implies that, in
271 nanoscale-confined systems, cation trapping occurring at the carbon surface level
272 may lead to a significant local depletion of ions, in particular potassium, at the
273 neuronal membrane/surface level.
274 Raman spectroscopy (sketched in Supplementary Fig. 5a) was performed on
275 supported SLG and MLG samples in liquid condition without and in the presence of
276 KCl and NaCl at physiological concentrations (4 mM and 150 mM, respectively) in
277 the solution. SLG Raman G-peak exhibited a change in shape and position in the
278 presence of NaCl and KCl D_2O solutions (Fig. 6a, left, inset) while in MLG it did not

279 change (Fig. 6a, right, inset). The mechanisms responsible for the observed shift in
280 the G Raman band of graphene with, more importantly, the narrowing of the G band
281 (FWHM) detected in SLG when samples are immersed in a KCl solution could result
282 from charge doping [40] or internal strain [41]. More specifically, the shifts in G-band
283 position exhibited by SLG in the presence of salt solutions could be indicative of a
284 specific cation interaction, not measurable in MLG. Notably, the larger G-band
285 Raman shift in KCl-treated samples (3 ± 0.5 cm^{-1}) than in the presence of NaCl ($1 \pm$
286 0.5 cm^{-1}) correlates well with a larger SLG affinity for hydrated K^+ when compared to
287 Na^+.

288 Importantly, in our experimental settings, the specific cation-π interaction at
289 surface level could result in partial K^+ depletion from the extracellular solution facing
290 the cell membrane (Fig. 6b) due to the tiny thickness of the cleft (see Supplementary
291 Information and Fig. S6) between cells and substrates.

292

293 **Substrate modulation of graphene cation-π interaction**

294 Our experiments have shown that SLG behaves differently from MLG in respect to
295 the K^+ homeostasis of neurons and subsequent improved excitability. The two
296 culturing platforms, SLG and MLG, differ only in the conductive properties of the
297 supporting structure immediately below the first mono-atomic carbon layer exposed
298 to the biological milieu (i.e., on one hand glass and on the other multiple layers of
299 graphene/graphite). From the point of view of a neuron growing on its top, MLG
300 appears as a SLG film layered on the underlying, electrically conductive, MLG. In our
301 hypothesis, graphene efficiency in trapping K^+ ions is tuned or influenced by the
302 electronic properties of the supporting structure [42,43].

303 We compared PSCs in neurons directly grown on glass (Control), on free-
304 standing SLG (suspended SLG, see Methods) and on SLG transferred on an
305 insulating substrate (SLG on glass) and on a conductive substrate of Indium Tin-
306 Oxide (SLG on ITO)[18]. The results of such experiments (Figure 6c) are in full
307 agreement with our hypothesis: the PSCs frequency was boosted by SLG on glass,
308 and even more by suspended SLG, with no detectable effects when SLG was
309 layered on ITO. Notably, in suspended SLG, PSCs amplitude is also significantly
310 higher than Control.
311 It is not trivial to understand the underlying exact mechanism, in the absence of any
312 theoretical model describing the dependency of graphene π-cation interaction on
313 supporting surface properties, we speculate that surface conductivity is playing a key
314 role. In particular, in suspended SLG, environmental disturbances are minimized
315 allowing access to the intrinsic properties of graphene close to the unperturbed Dirac
316 point. Superficial charge inhomogeneity is reduced in this case compared to
317 supported samples, giving rise to a “close-to-theory” system [1,44] (Fig. 6d, left) that
318 will fit better to cation-π simulations’ results [33,45,46]. SLG laying on metal surfaces
319 usually undergo electron-doping resulting in a down-shift of graphene Dirac point
320 [47] (Fig. 6d, middle). This will induce a homogeneous charge-distribution [48] that
321 could result in a reduction of graphene cation-π interaction force. On the other hand,
322 in SLG transferred on insulating substrates there are significant local fluctuations in
323 surface potential [49,50], thus inducing an inhomogeneous charge distribution on
324 graphene surface where neutral areas, where SLG band structure is basically
325 unperturbed as in the case of suspended graphene, and p-doped areas, coexist
326 [51,52]. In the latter case, graphene-K^+ interactions will still be present even if with
327 less pronounced effect than on suspended SLG. Our preliminary Raman results can

328 explain the different behaviour of SLG towards K^+ or Na^+ and the difference between
329 SLG and MLG behaviour in ion solution. However, they do not directly demonstrate
330 differences between SLG and MLG in ion absorbance.
331

332 **Conclusions**

333 SLG modifies neuronal excitability and we propose that this effect is mediated
334 by graphene ability to restrict K^+ ions mobility in close proximity to the material
335 surface, but only when SLG is deposited on electrically insulating substrates. We
336 cannot exclude additional mechanisms related to non-uniform charge carrier
337 densities, affecting surface concentrations of ions [53]. Alternatively, restricted ion
338 mobility might affect the way astrocytes regulate the extracellular *milieu* between
339 graphene and neurons.
340 Ultimately, we provided multiple lines of evidence to demonstrate that SLG, when
341 engineered on an insulating glass-substrate, is able to tune neuronal excitability. Our
342 physiological experiments demonstrate that the detected increase in neuronal
343 synaptic activity is caused by increased cell firing, rather than by changes in network
344 size, synaptic density [54,55,56], inhibition/excitation ratio or inhibition maturation.
345 We also demonstrated that neurons, exposed to SLG, up-regulate K^+ currents and
346 switch to functionally-*tonic* firing phenotypes. Our simulations support the notion that
347 changes in the ratio of *adapting*/*tonic* firing neurons will impact the global network
348 activity [57,58] and suggest the key contribution of up-regulated potassium currents
349 in driving this change. All these effects are not mimicked by MLG or other conductive
350 substrates, such as Au. We propose that, due to the cation-π interactions of
351 graphene, cations, and K^+ in particular [37,38,39], will be trapped at the graphene
352 surface, resulting in a graded ionic depletion at distances from the material

353 compatible with the nanometre-scale characterizing cell-adhesion mechanisms
354 [59,60]. This hypothesis is grounded in earlier molecular dynamics simulations at the
355 equilibrium [37], where ionic enrichment occurs at the interface.
356 Graphene properties might thus affect neuronal information processing *in virtue* of
357 the physical interactions of such a nanomaterial with the biological environment.
358 Novel materials might then represent, in general, unconventional tools to gain
359 insights into genuine biological processes.
360

361 **REFERENCES**

362 [1] Novoselov, K. S. et al. Electric Field Effect in Atomically Thin Carbon Films.
363 Science 306, 666-669 (2004).
364 [2] Geim, A. K. & Novoselov, K. S. The rise of graphene. Nat Mater. 6, 183-191
365 (2007).
366 [3] Yang, Y. et al. Graphene based materials for biomedical applications. Mat
367 Today 16, 365-373 (2013).
368 [4] Li, X., et al. Transfer of large-area graphene films for high-performance
369 transparent conductive electrodes. Nano Lett. 9, 4359-4363 (2009)
370 [5] Shin, S. R. et al. Graphene-based materials for tissue engineering. Adv Drug
371 Deliv Rev. 105, 255-274 (2016).
372 [6] Lu, Y. et al. Flexible Neural Electrode Array Based-on Porous Graphene for
373 Cortical Microstimulation and Sensing. Sci Rep. 6, 33526 (2016).
374 [7] Herbert, C. et al. Flexible graphene solution-gated field effect transistors,
375 efficient transducers for micro-electrocorticography Adv. Funct. Mater.28,
376 1703976 (2017).

377 [8] Kim, J. et al. Monolayer Graphene-Directed Growth and Neuronal
378 Differentiation of Mesenchymal Stem Cells. J Biomed Nanotechnol. 11, 2024-
379 2033 (2015).
380 [9] Fabbro, A. et al. Graphene-Based Interfaces Do Not Alter Target Nerve Cells.
381 ACS Nano 10, 615-623 (2016).
382 [10] Rauti, R. et al. Graphene Oxide Nanosheets Reshape Synaptic Function in
383 Cultured Brain Networks. ACS Nano 10, 4459-4471 (2016).
384 [11] Famm, K. et al. Drug discovery: a jump-start for electroceuticals. Nature
385 496, 159-161 (2013).
386 [12] Rivnay, J. et al. Next-generation probes, particles, and proteins for neural
387 interfacing. Sci Adv. 3, e1601649 (2017).
388 [13] Cançado, L.G. et al. Quantifying defects in graphene via Raman
389 spectroscopy at different excitation energies. Nano Lett. 11, 3190-3196 (2011).
390 [14] Kim, J. et al, Monolayer Graphene-Directed Growth and Neuronal
391 Differentiation of Mesenchymal Stem Cells. J Biomed. Nanotechnol. 11, 2024-
392 2033 (2015).
393 [15] Baldrighi, M. et al, Carbon Nanomaterials Interfacing with Neurons: An In
394 vivo Perspective. Front. Neurosci. 10, 250 (2016).
395 [16] Lovat, V. et al. Carbon nanotube substrates boost neuronal electrical
396 signaling. Nano Lett. 5, 1107-1110 (2005).
397 [17] Cellot, G. et al. Carbon nanotubes might improve neuronal performance by
398 favouring electrical shortcuts. Nat. Nanotechnol. 4, 126-133 (2009).
399 [18] Cellot, G. et al, Carbon nanotube scaffolds tune synaptic strength in cultured
400 neural circuits: novel frontiers in nanomaterial-tissue interactions. J. Neurosci.
401 31, 12945-12953 (2011).

402 [19] Raastad, M. et al. Putative Single Quantum and Single Fibre Excitatory
403 Postsynaptic Currents Show Similar Amplitude Range and Variability in Rat
404 Hippocampal Slices. Eur J Neurosci. 4, 113-117 (1992).
405 [20] Pampaloni, NP. et al. Sculpting neurotransmission during synaptic
406 development by 2D nanostructured interfaces. Nanomedicine. S1549-9634,
407 30082-5 (2017).
408 [21] Arosio, D. & Ratto, GM. Twenty years of fluorescence imaging of
409 intracellular chloride. Front Cell Neurosci. 8, 258 (2014).
410 [22] Cherubini, E. GABA mediated excitation in immature rat CA3 hippocampal
411 neurons. Int J Dev Neurosci. 8, 481-90 (1990).
412 [23] Marandi, N., Konnerth, A. & Garaschuk O. Two-photon chloride imaging in
413 neurons of brain slices. Pflugers Arch. 445, 357-65 (2002).
414 [24] Ruscheweyh, R. & Sandkuhler, J. Lamina-specific membrane and discharge
415 properties of rat spinal dorsal horn neurones in vitro. J Physiol. 541, 231-244
416 (2002).
417 [25] Chang, YM. & Luebke, JI. Electrophysiological diversity of layer 5 pyramidal
418 cells in the prefrontal cortex of the rhesus monkey: in vitro slice studies. J
419 Neurophysiol. 98, 2622-32. (2007)
420 [26] Routh, B. N. et al. Anatomical and Electrophysiological Comparison of CA1
421 Pyramidal Neurons of the Rat and Mouse. J Neurophysiol. 102, 2288–2302
422 (2009).
423 [27] Renganathan, M., Cummins, TR. & Waxman, SG. Contribution of Na(v)1.8
424 sodium channels to action potential electrogenesis in DRG neurons. J
425 Neurophysiol. 86, 629-40 (2001).

426 [28] Platkiewicz, J. & Brette, R. Impact of Fast Sodium Channel Inactivation on
427 Spike Threshold Dynamics and Synaptic Integration. PLoS Comput Biol. 7,
428 e1001129 (2011).
429 [29] Kress, G. J. et al. Axonal sodium channel distribution shapes the
430 depolarized action potential threshold of dentate granule neurons. Hippocampus
431 20, 558-571 (2016).
432 [30] Storm, J. F. Action potential repolarization and a fast after-hyperpolarization
433 in rat hippocampal pyramidal cells. J Physiol. 385, 733-759 (1987).
434 [31] Sah, P. & Faber, E. S. Channels underlying neuronal calcium-activated
435 potassium currents. Prog Neurobiol. 66, 345-353 (2002).
436 [32] Dégenètais, E. et al. Electrophysiological properties of pyramidal neurons in
437 the rat prefrontal cortex: an in vivo intracellular recording study. Cereb Cortex 12,
438 1-16 (2002).
439 [33] Furlan, F. et al. ERG conductance expression modulates the excitability of
440 ventral horn GABAergic interneurons that control rhythmic oscillations in the
441 developing mouse spinal cord. J. Neurosci. 27, 919-928 (2007).
442 [34] Marom, S. & Shahaf, G. Development, learning and memory in large random
443 networks of cortical neurons: lessons beyond anatomy. Q Rev Biophys. 35, 63-
444 87 (2002).
445 [35] Sterratt, D. Principles of computational modelling in neuroscience.
446 Cambridge University Press(2011).
447 [36] Kumpf R A, & Dougherty D A. A mechanism for ion selectivity in potassium
448 channels: computational studies of cation-pi interactions. Science. 261, 1708-10
449 (1993).

450 [37] Shi, G, et al. Ion enrichment on the hydrophobic carbon-based surface in
451 aqueous salt solutions due to cation-π interactions. Sci Rep., 3, 3436 (2013).
452 [38] Pham T A, et al. Salt Solutions in Carbon Nanotubes: The Role of Cation−π
453 Interactions J. Phys. Chem. C, 120, 7332-7338 (2016).
454 [39] Williams, C D, et al. Effective Polarization in Pairwise Potentials at the
455 Graphene–Electrolyte Interface J. Phys. Chem. Lett., 8, 703-708 (2017)
456 [40] Dong, X et al. Doping single-layer graphene with aromatic molecules. Small.
457 5, 1422-6 (2009)
458 [41] Chacón-Torres, JC, Wirtz, L, Pichler, T. Manifestation of charged and
459 strained graphene layers in the Raman response of graphite intercalation
460 compounds. ACS Nano. 7, 9249-59 (2013).
461 [42] Novák M, et al. Solvent effects on ion-receptor interactions in the presence
462 of an external electric field. Phys Chem Chem Phys. 18, 30754-30760 (2016).
463 [43] Chen, K. et al, Electronic Properties of Graphene Altered by Substrate
464 Surface Chemistry and Externally Applied Electric Field. J. Phys. Chem. C, 116,
465 6259-6267 (2012)
466 [44] Novoselov, K. et al., Two-dimensional gas of massless Dirac fermions in
467 graphene. Nature. 438, 197-200 (2005).
468 [45] Gigante, G. et al. Network Events on Multiple Space and Time Scales in
469 Cultured Neural Networks and in a Stochastic Rate Model. PLoS Comput Biol.
470 11, e1004547 (2015).
471 [46] Gambazzi, L. et al. Diminished activity-dependent brain-derived neurotrophic
472 factor expression underlies cortical neuron microcircuit hypoconnectivity resulting
473 from exposure to mutant huntingtin fragments. J. Pharmacol Exp Ther. 335, 13-
474 22 (2010).

[47] González-Herrero, H et al. Graphene Tunable Transparency to Tunneling Electrons: A Direct Tool to Measure the Local Coupling. ACS Nano. 10, 5131-44 (2016).

[48] Praveen, C. S. et al., Adsorption of alkali adatoms on graphene supported by the Au/Ni(111) surface, Phys Rev. B 92, 075403 (2015).

[49] Kang, Y-J. et al. Electronic structure of graphene and doping effect on SiO_2 Phys Rev. B 78, 115404 (2008).

[50] Miwa, R. H. et al. Doping of graphene adsorbed on the a-SiO_2 surface. Appl Phys Lett 99, 163108 (2011).

[51] Ao, Z. et al. Density functional theory calculations on graphene/α-SiO2(0001) interface. Nanoscale Res Lett. 7, 158 (2012).

[52] Fan, X. F. et al. Interaction between graphene and the surface of SiO_2. J Phys Condens Matter. 24, 305004 (2012).

[53] Hille, B. Ion channels of excitable membranes. Sunderland, Mass: Sinauer, (2001).

[54] Slomowitz, E. et al. Interplay between population firing stability and single neuron dynamics in hippocampal networks. eLife 4, e04378 (2015).

[55] Bogaard, A. et al. Interaction of cellular and network mechanisms in spatiotemporal pattern formation in neuronal networks. J Neurosci. 29, 1677-1687 (2009).

[56] Sahasranamam, A. et al. Dynamical state of the network determines the efficacy of single neuron properties in shaping the network activity. Sci Rep. 6, 26029 (2016).

498 [57] Radulescu, R.A. Mechanisms Explaining Transitions between Tonic and
499 Phasic Firing in Neuronal Populations as Predicted by a Low Dimensional Firing
500 Rate Model. PLoS One 5, e12695 (2010).
501 [58] Naud, R. et al. Firing patterns in the adaptive exponential integrate-and-fire
502 model. Biol Cybern. 99, 335-347 (2008).
503 [59] Wrobel G, Höller M, Ingebrandt S, Dieluweit S, Sommerhage F, Bochem HP,
504 Offenhäusser A. Transmission electron microscopy study of the cell-sensor
505 interface. J R Soc Interface. 5, 213-222. (2008).
506 [60] Braun, D. & Fromherz, P. Fluorescence interference-contrast microscopy of
507 cell adhesion on oxidized silicon. Appl Phys A 65, 341-348 (1997).
508 [61] Ferrari A. C. et al. Raman spectrum of graphene and graphene layers. Phys.
509 Rev. Lett. 97, 187401 (2006).
510 [62] Cançado, L. G. et al. Measuring the degree of stacking order in graphite by
511 Raman spectroscopy. Carbon 46, 272-275 (2008).
512 [63] Alagem, N. et al, Mechanism of Ba(2+) block of a mouse inwardly rectifying
513 K+ channel: differential contribution by two discrete residues. J Physiol. 534,
514 381-393 (2001).
515 [64] Alger, B. E. & Nicoll, R. A. Epileptiform burst afterhyperolarization: calcium-
516 dependent potassium potential in hippocampal CA1 pyramidal cells. Science
517 210, 1122-1124 (1980).
518 [65] Jiang, Y. & MacKinnon, R. The barium site in a potassium channel by x-ray
519 crystallography. J Gen Physiol. 115, 269-272 (2000).
520 [66] Nisenmbaum, E. S. & Wilson, C. J. Potassium currents responsible for
521 inward and outward rectification in rat neostriatal spiny projection neurons. J
522 Neurosci. 15, 4449-4463 (1995).

[67] Pisirowski, R. & Aldrich, R. W. Calcium activation of BK(Ca) potassium channels lacking the calcium bowl and RCK domains. Nature. 420, 499-502 (2002).

[68] Stocker, M. et al, An apamin-sensitive Ca^{2+}-activated K^{+} current in hippocampal pyramidal neurons. Prot Nat Acad Sci. 96, 4662-4667(1999).

[69] Hodgkin, A. L. & Huxley, A. F. A quantitative description of membrane current and its application to conduction and excitation in nerve. J Physiol. 117, 500-544 (1952).

[70] French, C. R. et al. Properties of an intermediate-duration inactivation process of the voltage-gated sodium conductance in rat hippocampal CA1 neurons. J Neurophysiol. 115, 790-802 (2016).

Acknowledgement

We are grateful to M. Lazzarino, S. Dal Zilio and the Facility of NanoFabrication of IOM of Trieste for experimental assistance in the fabrication of suspended SLG and FIB analysis; N. Secomandi and R. Rauti for assistance in imaging. We thank A. Laio, G. Scoles, A. Nistri and B. Cortés-Llanos for helpful discussion. This paper is based on work supported by the European Union Seventh Framework Program under grant agreement no. 696656 Graphene Flagship and no. 720270 Human Brain Project Flagship, and by the Flanders Research Foundation (grant no. G0F1517N). MP, as the recipient of the AXA Chair, is grateful to the AXA Research Fund for financial support. MP was also supported by the Spanish Ministry of Economy and Competitiveness MINECO (project CTQ2016-76721-R), by the University of Trieste and by Diputación Foral de Gipuzkoa program Red (101).

548

549 **Author Contributions**

550 N.P.P. performed electrophysiological experiments, imaging, immunochemistry,
551 confocal microscopy and all the related analysis; M.L. fabricated supported SLG
552 and MLG and performed all material characterization; M.G. performed
553 mathematical simulations and analysis and contributed to the writing of the
554 manuscript; A.M. fabricate suspended SLG and gold plated samples; F.D.A. and
555 A.M. performed Raman experiments and data analysis on SLG and MLG in wet
556 and dried conditions; M. P., D.S. and L.B. conceived the study; D.S., L.B., and
557 J.A.G. designed the experimental strategy, interpreted the results and wrote the
558 manuscript.
559 All authors discussed the results and commented on the manuscript.

560

561 **Competing financial interests**

562 The authors declare no competing financial interests.

563

564 **FIGURE LEGENDS**

565 **Figure 1 | Characterization of the substrates. a**, AFM topography reconstructions
566 of glass control, SLG, MLG and gold plated glass surfaces. AFM documented a
567 surface roughness of the materials that varied from 0.23 ± 0.02 nm in Control (n = 3
568 samples), 1.5 ± 0.5 nm in SLG (n = 3 samples), 20 ± 10 nm for MLG (n = 3 samples)
569 and 0.47 ± 0.1 nm for Au (n = 3 samples). Scale bar: 5 μm. **b**, Spatial maps of the
570 2D/G and D/G peak amplitude ratio maps. Scale bar: 10 μm. The single punctual
571 Raman spectra of SLG (in red) and MLG (in blue) represent mapping data points
572 with the corresponding average peak amplitude ratios. On the right, relative spatial

573 2D/G and D/G ratio maps. The FWHM of the 2D peak, as well as the I_{2D}/I_G ratio are
574 indicative of a low bilayer content in the case of SLG [61] and turbostratic graphite in
575 the case of MLG [62]. A graphitic Raman signature is to be expected as the MLG
576 samples have a typical thickness of a few hundreds of layers. **c**, XPS spectrum (X-
577 Ray source: Mg Kα) of SLG (in red) and MLG (in blue) on Si_3N_4. Dotted lines
578 highlight the relevant elements, while the unlabelled features around 750 eV and 980
579 eV correspond to the oxygen KL_1L_1 and the carbon KVV Auger lines respectively.
580

581 **Figure 2 | Single-Layer graphene increase neuronal network activity. a**,
582 Representative SEM micrographs depicting hippocampal neurons morphology after
583 10 DIV, supported by the different substrates (n = 5 fields each). Culture substrates
584 were not pre-treated with any additional adhesion molecules, which might mask the
585 effects of graphene. Scale bar: 10 μm. **b**, Representative fluorescent microscopy
586 images showing dissociated hippocampal networks labelled with class III β-tubulin
587 (for neurons) in red and GFAP (for astrocytes) in green. Scale bar: 100 μm.
588 The histograms show the density of cells (top) and the neuron/glia ratio (bottom)
589 across all four conditions, which did not significantly differ (n = 30 fields, 3 culture
590 series, each). In addition, SLG or MLG topography did not influence neuronal fibres'
591 orientation in respect to Control or Au (see Methods). These observations, combined
592 to the similarity of membrane passive electrical properties (see Methods), indicated
593 the homogeneous growth of healthy neurons [17] across substrates, with
594 comparable levels of cellular composition and organization. **c**, Representative traces
595 of the spontaneous network activity of neurons grown on the different substrates are
596 shown (left), the corresponding isolated PSCs are shown superimposed (middle; in
597 black the average values). Box plots summarize the PSC amplitude values (right,

598 top) and the PSC frequency ones (right, bottom) in all experimental conditions (SLG,
599 n = 45; MLG, n = 20; Au, n = 20; Control, n = 40). Note the significantly higher PSC
600 frequency in SLG than all other substrates (i.e., Control 1.53 ± 0.22 Hz; SLG 3.21 ±
601 0.41 Hz; P=0.0010). Differences between the variables were assessed using one-
602 way ANOVA and multiple comparisons were adjusted by Bonferroni correction.
603
604 **Figure 3 | Single-layer graphene does not increase the number of synapses**
605 **and the network composition. a**, Exemplificative traces of spontaneous synaptic
606 activity, recorded in the presence of TTX, are shown together with their
607 superimposed mPSCs (right, in black the average values). Control (n = 11) and SLG
608 (n = 11) mPSC frequency and amplitude are summarized in the box plots, note that
609 no differences were detected in these parameters. **b**, Confocal images of neuronal
610 cultures (10 DIV) in Control and SLG identifying the presynaptic VGlut1 (in green) in
611 III β-tubulin positive cells (orange). Scale bar: 20 μm. Higher magnifications of the
612 region highlighted by white boxes are displayed for clarity. Scale bar: 5 μm. The
613 histograms on the right summarize VGlut1 puncta densities in the two conditions (5.2
614 ± 1.14 a.u. in Control and 4.5 ± 0.64 a.u. in SLG; P = 0.207, n = 30 fields, 3 cultures
615 each). **c**, Confocal images of neuronal cultures (10 DIV) in Control and SLG
616 identifying positive cells for class III β-tubulin and GABA. Scale bar: 10 μm. The
617 histograms on the right summarize the percentage of double-positive cells in the two
618 conditions (33 ± 2.7 % in Control and 30 ± 2.5 % in SLG; P = 0.21, n= 20 fields
619 each). Statistically significant difference between two data sets was assessed by
620 Student's t test for parametric data and by Mann-Whitney for non-parametric ones.
621

622 **Figure 4 | SLG triggers changes in single cell intrinsic excitability. a**,
623 Representative current-clamp recordings of hippocampal neurons in culture (10 DIV)
624 in Control and SLG. Control and SLG neurons displayed similar resting membrane
625 potentials (–52 ± 10 mV in SLG; –50 ± 7 mV in Control). When hold at –60 mV, the
626 cell's spontaneous AP firing was measured as summarized in the histograms (right).
627 Note the significantly higher AP frequency in SLG (2.60 ± 0.36 Hz in SLG, n = 21;
628 1.37 ± 0.26 Hz in Control, n = 19; P = 0.0054). **b**, Evoked single AP in Control (top)
629 and SLG (bottom). Note the pronounced AHP in SLG neurons, that was partially
630 abolished by each of the treatments shown: BaCl, TEA or Apamin (right,
631 superimposed tracings). The histogram quantifies the area below the Control and
632 SLG post-AP voltage trajectories with respect to the resting membrane potential. The
633 AHP in SLG neurons was significantly different than the ADP detected in control
634 neurons (–86.96 ± 23.60 mV·ms in SLG, n = 25; +107.12 ± 21.85 mV·ms in Control,
635 n = 20; P = 0.0010). Interestingly, the AHP was reduced (by 88%) by bath applying
636 Ba^{++} ($BaCl_2$, 2 mM; n = 3), which is known to block K_{ir} and K_{Ca} membrane channels
637 [63,64,65,66]. The AHP was also reduced (by 58%) by bath applying tetra-
638 ethylammonium (TEA, 1 mM; n = 9) a non-selective blocker of the large majority of
639 voltage gated K^+ membrane channels (K_v) [30], including BK_{Ca} channels [67]. Finally,
640 Apamin (200 μM; n = 5), a specific inhibitor of SK_{Ca} membrane channels [68], also
641 strongly affected (47% reduction) the AHP. **c**, Current-clamp recordings from
642 neurons in control and SLG revealed different cell discharge patterns, classified as
643 *adapting* or *tonic*. **d**, Bar charts illustrate probability distributions (expressed as
644 percentage of sampled population) of each cell type in Control (n = 13) and SLG (n =
645 15) cultures. Note that in Control 81.8% are *adapting* and in SLG 83.3% are *tonic*. **e**,
646 Scatter plot of after-potential area *vs*. the number of action potentials (APs) in SLG

647 neurons when a single AP is elicited (as in b; open circle) or when multiple APs are
648 evoked (as in c, filled circle) by 1 s long depolarizing step (–352 ± 70 mV·ms upon
649 long depolarizing steps). **f**, Representative records of voltage-activated outward
650 currents evoked by depolarizing current steps in Control and SLG (capacitive
651 transients were not removed). Plot summarizes the I/V relation in Control (n = 13)
652 and SLG (n = 15) neurons obtained upon subtraction of leak currents. Note that SLG
653 outward currents were significantly larger than control ones (10 mV step, P=0.032;
654 20 mV step, P=0.031; 30 mV step, P=0.019). Statistically significant difference
655 between two parametric data sets was assessed by Student's t test.
656
657 **Figure 5 | Spike-rate network model.** The electrical activity of excitatory and
658 inhibitory recurrently interacting neurons was described by a mathematical model
659 (see Supplemental Methods). **a**, The increase in the fraction of non-adapting
660 neurons, observed *in vitro* on graphene substrates, predicts a higher rate of
661 occurrence *in silic*o for spontaneous "bursts" of spikes, synchronized across the
662 network. These bursts are presynaptic correlates of the synaptic potentials, observed
663 experimentally by voltage-clamp. **b** and **c**, Samples of the simulated network firing
664 rates, analysed in **a**, are shown for two fractions of non-adapting neurons, *i.e.* 20%
665 and 80%, out of the total of excitatory neurons. **d**, Counter-intuitive effects of outward
666 potassium currents on cell excitability are explored in a single-cell biophysical model
667 (parameters as in Table 2). As a proof of concept, we considered the simplest
668 possible model of AP generation, as proposed by Hodgkin and Huxley (HH) [69].
669 This model describes the generation of a (train of) AP(s) in terms of the known
670 interplay between fast-inactivating (~1 ms) inward Na^+ currents and delayed rectifier
671 outward K^+ potassium currents –of course, by no means these are the only

membrane currents underlying the electrophysiological behaviour of rat hippocampal neurons [70]. The membrane potential responses (black traces) to an external step current was simulated, as in the experiments (see Methods). **d** and **e**, Plots within each panel exemplify how an increase (from left to right subpanels) of the maximal K^+ conductance or, in **f**, its driving force, through a depletion of extracellular K^+ ions, may to some extent reverse the inactivation of inward Na^+ currents (green traces in **d**). Then, inactivating neuronal responses may turn into sustained firing thereby increasing cell excitability (as in **c**). All in all, this suggests a specific involvement of the extracellular concentration of K^+ in neuronal excitability: the less extracellular K^+ the higher the excitability, at least in those regimes where progressive sodium inactivation affects neuronal firing disfavoring sustained *tonic* response. Parameters: in **d**, G_K in {0.012; 0.0216} mS/mm^2; in **e**, G_K in {0.012, 0.04, 0.06} mS/mm^2 from left to right, I_{stim} 5 nA/mm^2; in **f**, I_{stim} as in **e**, while E_K in {-75, -77.6, -80.5} mV from left to right, corresponding to a {0%, 10%, 20%} depletion of extracellular K^+ ions.

Figure 6 | Graphene deplete potassium at the cell/substrate cleft. a, Graphene-related G vibrational peak [61] was evaluated in wave number position for both SLG (left) and MLG substrates (right) with samples totally immersed in pure deuterium oxide (D_2O), in D_2O solution containing 4 mM KCl, and in D_2O solution containing 150 mM NaCl (see Supplementary Methods for technical details). The wavenumber maximum position relative to the G-peak Raman shift for control SLG sample was collocated at 1599 ± 0.5 cm^{-1}. It exhibited a change in shape associated to a G-peak position shift to 1600 ± 0.5 cm^{-1} and to 1602 ± 0.5 cm^{-1} in the presence of NaCl and KCl D_2O solutions, respectively (left, inset). Conversely, in MLG samples G peak maximum position did not change (right, inset). **b**, Sketch of the local amount of K^+

697 depletion in the membrane/surface cleft due to graphene trapping as function of cleft
698 thickness. In light green the extrapolated values of such a distance (40÷100 nm)
699 [34]. See Supplementary methods for technical details. **c**, Box plots summarize the
700 average PSC frequency values (left) and the average PSC amplitudes ones (right)
701 for neurons developed on glass control (in grey, n = 21), on glass supported SLG (in
702 red, n = 21), on free-standing SLG (in green, n = 26) and on SLG deposited on ITO
703 (in blue, n = 8). Note the significant increase in PSC frequency in SLG laying on
704 insulating glass than Controls (3.11 ± 0.35 Hz vs. 1.72 ± 0.21 Hz, P = 0.031) or,
705 even more, when grown on suspended SLG (4.22 ± 0.35 Hz vs. Controls, P =
706 0.001). SLG on conductive ITO does not change neuronal activity. Notably, in
707 suspended SLG, PSCs amplitude is also significantly increased (59.2 ± 5.8 pA *vs.*
708 35.9 ± 4.9 pA, P = 0.017) when compared to control cultures. **d**, Hypothesis of Dirac
709 point and Fermi level rearrangement as function of SLG supporting material
710 (bottom), and an exemplification of the possible charge distribution in graphene layer
711 as function of electrical characteristics of the underlying surface (top). Blue areas
712 represent more positive regions (e.g. depletion of electrons), red areas represent
713 more negative ones (e.g. persistency of electrons).
714 Differences between the variables were assessed using one-way ANOVA and
715 multiple comparisons were adjusted by Bonferroni correction.
716
717
718
719
720 **METHODS**
721 **Substrate fabrication**

722 SLG was CVD grown on ultra-flat Cu surfaces and transferred, as previously
723 described [1], onto SiO_2 and Si_3N_4 substrates for subsequent Raman and XPS
724 characterization. Briefly, after annealing the Cu foil in a 400 sccm :100 sccm argon
725 and hydrogen atmosphere at 100 mbar and 1015 °C, a SLG layer is nucleated at 15
726 mbar with 0.2 sccm methane and closed by successively increasing the methane
727 content to 0.5 sccm. The graphene is transferred using PMMA (PMMA 950K A2,
728 MicroChem, USA) or PS (Polystyrene MW ~192k, Sigma-Aldrich, USA). For
729 neuronal culturing, SLG was transferred to glass coverslips or indium tin oxide (ITO).
730 Before the transfer procedure, hosting substrates were ultrasonicated in acetone and
731 isopropanol to assure the required cleanness. Glass and ITO coverslips followed an
732 additionally cleaning step in concentrated HCl overnight. MLG sheets were CVD
733 grown on Ni ultra-flat surfaces as described previously [2] and transferred on hosting
734 substrates following the same procedure adopted for SLG. Briefly, the Ni foil was
735 annealed as described before, at a temperature of 900 °C. After annealing, a
736 methane flow of 10 sccm at 50 mbar enabled to the diffusion of carbon into the foil,
737 which then, during the following slow cooling step, precipitated to a layer of MLG on
738 the surface.
739 Gold samples have been prepared starting from glass rectangular slides (24 mm x
740 12 mm, 0.2 mm thick), cleaned previously in hot Piranha solution (H_2SO_4:H_2O_2, 5:5
741 ratio in volume) in order to remove eventually present organic contaminants.
742 Subsequently, 15 nm of Au were thermally evaporated at a rate of 0.5 Å/s. A thin
743 adhesion layer of 5 nm of Cr was used in order to improve Au/glass adhesion. A
744 quartz crystal microbalance was used as thickness control.
745 To obtain suspended graphene structures, graphene is transferred on patterned
746 substrates obtained using OrmoComp® (micro resist technology, GmbH), a flexible

747 and biocompatible inorganic-organic material. The OrmoComp® substrates have
748 been prepared on circular glasses (5 mm diameter, 0.12 mm thick), previously
749 cleaned in hot Piranha solution (H_2SO_4:H_2O_2 5:5 % v/v) in order to remove all
750 organic contaminants. Subsequently, a poly-dimethylsiloxane (PDMS) master is
751 prepared with replica molding process starting from a silicon stamp which is
752 patterned with an array of parallel lines of width and periodicity of 10 μm and 20 μm,
753 respectively. The PDMS master is used to press a drop of OrmoComp® on the
754 circular glass in order to transfer the micropattern. Finally, the OrmoComp® is cured
755 with UV light and the PDMS master is released. Commercially available single-layer
756 CVD graphene on copper (GRAPHENEA – San Sebastián, Spain) is wet-transferred
757 on the OrmoComp® substrates following the protocol described by Matruglio *et al.*
758 [3]. Briefly, a layer of 250 nm of mr-I 7020 (a thermoplastic polymer of Micro Resist
759 Technology GmbH) is used as sacrificial layer and spin coated on the graphene/Cu.
760 The polymer/graphene/Cu membrane is placed in a copper etching solution
761 ($FeCl_3$:H_2O 3:7 % v/v), etched overnight and finally washed in DI water in order to
762 remove any residual due to the etching solution. The transfer of graphene is
763 performed fishing the polymer/graphene/Cu membrane into the water directly on the
764 OrmoComp® substrate. The water is left to evaporate at room temperature for 2 h,
765 and mr-I 7020 is dissolved in cold acetone for 5 minutes. Critical point drying process
766 is performed in order to avoid the collapse of the suspended structures.
767

768 **Cell culture and electrophysiology**

769 Isolation of primary brain tissue was carried out in accordance with the
770 recommendations in the Guide for the Care and Use of Laboratory Animals of the
771 National Institutes of Health and the appropriate international and institutional

standards for the care and use of animals in research (Italian Ministry of Health, in agreement with the EU Recommendation 2007/526/CE). The protocols in this study and all performed experiments are approved by the local veterinary service and the institutional (SISSA) ethical committee, in accordance with the EU guidelines (2010/63/UE) and Italian law (decree 26/14).

Dissociated hippocampal cultures were obtained from neonatal rats (P0÷2) as previously described [4,5,6], and were plated on glass Control, SLG-, MLG- or Au-covered glass coverslips. As in our previous work with different carbon-based nanomaterial (e.g. carbon nanotubes, CNTs) [4,5,6], we did not pre-treat the culture substrates with any additional adhesion molecules, which might mask the effects of graphene. Cultured cells were incubated at 37 °C, 5% CO_2 in culture medium composed of Neurobasal-A (Thermo Fischer) containing B27 2% (Gibco) Glutamax 10 mM and Gentamycin 0.5 μM (Gibco), and used for experiments at 8÷10 days *in vitro* (DIV).

Somatic whole-cell patch clamp recordings were performed at room temperature (20÷22 °C) with pipettes (4÷7 MΩ) containing: 105 mM K gluconate, 20 mM KCl, 10 mM HEPES, 4 mM MgATP, 0.3 mM GTP, pH 7.35. The external saline solution contained: 150 mM NaCl, 4 mM KCl, 1 mM $MgCl_2$, 2 mM $CaCl_2$, 10 mM HEPES, 10 mM Glucose, pH 7.4. Under voltage-clamp mode we measured the neuronal passive membrane properties: input resistance and cell capacitance did not significantly differ between the four groups (in Control 592 ± 51 MΩ, 74 ± 5 pF, n = 47; in SLG 664 ± 57 MΩ, 83 ± 4 pF, n = 54; in MLG 614 ± 74 MΩ, 85 ± 5 pF, n = 18; in Au 656 ± 65 MΩ, 80 ± 6 pF, n = 17). In voltage-clamp experiments, the holding potential (V_h) was –56 mV, not corrected for liquid junction potential, that was calculated to be –14

796 mV in our experimental conditions; the uncompensated value for series resistance
797 (Rs) was < 8÷11 MΩ.
798 Single spontaneous synaptic events (PSCs) and miniature PSCs (mPSCs) were
799 detected by the use of the AxoGraph X (Axograph Scientific) event detection
800 program and by the Clampfit 10 software (pClamp suite, Axon Instruments). On
801 average, ≥ 400 events were analysed from each cell in order to obtain mean
802 frequency and amplitude parameters. Glutamate AMPA-receptor and $GABA_A$-
803 receptor mediated PSCs were isolated offline by building two templates with different
804 kinetic parameters: respectively 0.1 ms rise-time; 3 and 30 ms decay time constant
805 (τ); 10 and 100 ms template length. Previous work [6,7] indicated that in our
806 experimental conditions, the vast majority of fast-decaying (τ < 5 ms) PSCs are
807 mediated by the glutamate AMPA-receptor type; while the slow-decaying (τ > 20 ms)
808 PSCs are mediated by the $GABA_A$-receptor type.
809 Current-voltage relations (I/V plots) were obtained by applying hyperpolarizing or
810 depolarizing voltage steps (15 steps of ΔV = 10 mV; 500 ms duration) from –110 mV
811 to +30 mV (values corrected for liquid junction potential) in the presence of 1 μM
812 Tetrodotoxin (TTX; Latoxan). A least square routine was fitted to the linear part of the
813 I/V curve, the slope of which was used to calculate leak conductance. Assuming that
814 a leak conductance is time and voltage independent, the I/V plot were corrected for
815 leak currents by subtracting the observed currents from the extrapolated leak
816 currents at the same level of test potential and the current values were then
817 normalized to the cell capacitance [8].
818 In current-clamp recordings, bridge balancing was continuously monitored and
819 adjusted. Action potentials (APs) were isolated off line by setting an appropriate
820 threshold voltage (10 mV). The fast voltage transients that crossed this value were

821 identified as APs and the spontaneous firing frequency for each neuron was
822 calculated on a sample of at least 5 min of continuous recording keeping (by
823 negative current injection) at –60 mV the resting membrane potential.
824 At –60 mV resting membrane potential, the AP properties were experimentally
825 determined by depolarizing (from 0 to 200 pA, in 20 pA increments) current steps
826 (500 ms). The first AP produced by the current-clamp series was used for single AP
827 measurements, including amplitude, threshold, duration at half-amplitude and
828 maximal rising slope [9,10,11]. The threshold for firing was determined by measuring
829 the voltage at the upward deflection of the trace, maximal AP amplitude was
830 measured from threshold to the peak of the spike, the duration was measured at
831 half-amplitude from threshold to peak and the maximal rising slope was measured as
832 max dV/dt in the selected area of the voltage tracings (all measures performed by
833 Clampfit; pClamp suite, 10.2 version; Axon Instruments). From this analysis, no
834 significant difference was found between Control (n = 21) and SLG (n = 19) groups
835 (amplitude: 56.4 ± 3.5 mV for Controls and 59 ± 3.1 mV in SLG, P = 0.57; width: 3.5
836 ± 0.25 ms for Controls and 3.7 ± 0.38 ms for SLG, P = 0.59; threshold: –34.2 ± 1.5
837 mV Control and –35.5 ± 1.2 mV in SLG, P=0.34; maximal rise slope: 61.6 ± 7.5
838 mV/ms Control and 57.3 ± 5.8 mV/ms in SLG, P= 0.32).
839 In evoked APs, the AHP was quantified over a window of 100 ms by calculating the
840 area below or above the voltage curve, starting 20 ms after the beginning of the AP.
841 AP discharge patterns were investigated by delivering depolarizing current steps (1
842 s) of 200 pA while keeping the cells at –60 mV resting potential with steady
843 intracellular current injection. “Adapting” and “tonic” responses were identified as
844 previously described [12].

845 Beside the monitoring of the spontaneous firing frequency, all the current clamp
846 experiments were carried out in presence of the synaptic blockers (all from Sigma)
847 CNQX (10 μM), Gabazine (5 μM) and APV (50 μM) added to the external solution.
848 Current and voltage clamp responses were digitized at 20 kHz with the pCLAMP 10
849 software (Molecular Devices) and stored for further analysis.
850

851 **Immunohistochemistry**

852 Hippocampal neurons were fixed with 4% formaldehyde (prepared from fresh
853 paraformaldehyde) in PBS for 20 min, permeabilized with 0.3% Triton-X-100 for 10
854 min and subsequently incubated with primary antibodies for 30 min at RT. After
855 washing in PBS cultures were then incubated with secondary antibodies for 45 min
856 and then mounted in *Vectashield* (Vector Laboratories) on 1 mm thick microscope
857 glass slides. As primary antibodies were used rabbit polyclonal anti-β-tubulin III
858 (Sigma T2200, 1:250 dilution), mouse monoclonal anti-GFAP (Sigma-Aldrich,
859 1:200 dilution), and guinea pig anti-vesicular glutamate transporter 1 (VGLUT1;
860 Millipore, 1:2000). As secondary antibodies were used Alexa 594 goat anti rabbit
861 (Invitrogen, dilution 1:500), Alexa 488 goat anti mouse (Invitrogen, dilution 1:500),
862 and Alexa 488 goat anti guinea-pig (Invitrogen, 1:500). To stain cells nuclei, we
863 used DAPI (Invitrogen, 1:200 dilution). To quantify cell density, images were
864 acquired with an Epifluorescence Microscope (DM 6000, Leica; 10× objective). We
865 collected 10 fields (1000 μm × 500 μm) per coverslip and analysed fluorescence
866 signals using ImageJ software (http://rsb.info.nih.gov/ij/).
867 To evaluate the orientation of the re-growing axons on the various substrates, we
868 quantified their relative orientation based on the directionality analysis [13]. Briefly,
869 the mean fibre's relative dispersion was computed from n = 5 randomly sampled

870 images per condition (Control, SLG, MLG and Au) where neuronal processes were
871 visualized by class III β-tubulin immunofluorescence (Fig. 2a). The analysis was
872 carried out using the Directionality plugin of Fiji software inferring the preferred
873 orientation of “structures” present in the input image. Fibre orientation was calculated
874 via a Fourier component analysis. We found no significant differences in the direction
875 of the mean fibre’s dispersion among different conditions (Control = 30 ± 9°; SLG =
876 29 ± 7°; MLG = 38 ± 8°; Au = 35 ± 9°) indicating a negligible impact of the substrate
877 on the orientation of the neuronal processes.
878 To quantify VGlut1 puncta, n = 20 ± 10 z-stacks (acquired every 0.4 μm) were taken
879 from n = 10 randomly selected fields (160 μm × 80 μm) per coverslip using an
880 inverted confocal Microscope (Nikon Eclipse Ti-E; 40x oil immersion objective, 1.3
881 NA). We selected only VGlut1-positive puncta (< 2 μm^3) co-localized with β-tubulin III
882 positive signal. For each image VGlut1 puncta were normalized to the β-tubulin III
883 positive volume. Images were analysed using the Volocity software (Perkin Elmer).
884 To highlight GABAergic neurons, cultures were stained with anti-GABA polyclonal
885 primary antibody produced in rabbit (SIGMA, A2052: 1:500). To label the NKCC1
886 co-transporter, we used anti NKCC1 rabbit polyclonal primary antibody (Abcam;
887 AB59791; 5 μg/mL). Cultures were then stained with class III β-tubulin primary
888 antibody produced in mouse (SIGMA; T5076; 1:500). As secondary antibody, we
889 used AlexaFluor 488 goat anti rabbit (ThermoFisher A11034; 1:500), and
890 AlexaFluor 594 goat anti mouse (ThermoFisher, A11032; 1:500).
891 To quantify the percentage of GABA-positive neurons, 10 ± 5 confocal z-stack
892 (Nikon PlanFluor 40× / 1.3 NA) were acquired from randomly selected fields and
893 GABA-positive neurons were counted. This value was then normalized to the
894 overall number of neurons (class III β-tubulin positive cells) for each field. To

895 quantify NKCC1 puncta, n = 10 z-stacks (acquired every 0.25 μm) were taken
896 from selected fields (106 μm × 106 μm) each group, using an inverted confocal
897 Microscope (Nikon Eclipse Ti-E; Nikon Plan Apo Lambda 60x oil immersion
898 objective, 1.4 NA). To quantify the amount of neuron-related NKCC1, only
899 NKCC1-positive puncta in contact with the β-tubulin III signal were selected.
900

901 **Imaging**

902 For Cl^- imaging experiments, primary hippocampal cultures (DIV 8÷10) were
903 loaded with the fluorescent Chloride indicator MQAE (Abcam; ab145418) diluted in
904 the standard extracellular solution at a final concentration of 1 mM for 10 min at 37
905 °C in the cell culture incubator. Samples were then washed in the extracellular
906 solution for 10 min at 37 °C. Samples were placed in a recording chamber
907 mounted on an inverted microscope (Nikon Eclipse Ti-U) and observed with a 60×
908 objective (0.7 NA, PlanFluor, Nikon). Images (1024 × 1024 pixels) from fields
909 containing 7 ± 4 neurons were acquired for 2 minutes at 5 Hz by a Hamamatsu
910 Orca-Flash 4.0 digital camera, exciting the MQAE dye at the 365 nm Hg peak
911 using a UV-2A Nikon filter set. Excitation light was attenuated by a neutral density
912 filter (ND 16). Images of emitted fluorescence (>420 nm) were displayed on a
913 colour monitor controlled by an integrating imaging software package (HCImage,
914 Hamamatsu) using a personal computer. Recorded images were analysed offline
915 with the Clampfit software (pClamp suite, 10.2 version; Axon Instruments). Image
916 time stacks were analysed in selected region of interest (ROI) to measure the
917 variations in MQAE fluorescence intensity. Intracellular Cl^- transients were
918 expressed as fractional amplitude variations ($\Delta F/F_0$, where F_0 is the baseline
919 fluorescence level and ΔF is the change over the baseline); the onset time of

920 neuronal activation determined by detecting those events in the fluorescence
921 signal that exceed at least five times the standard deviation of the noise. To elicit
922 chloride influx/efflux through the membrane, an injection pipette (patch pipette with
923 resistance of 1÷4 MΩ, filled with 10 mM GABA diluted in the extracellular solution)
924 was positioned at 20÷50 μm from the cell soma and connected to a pico-spritzer
925 (PDES-02DX, npi Electronics) with 1 psi in-line pressure. 500 ms GABA puffs
926 were delivered at fixed times. At the beginning of each experiment, a pipette
927 containing pure saline was used to exclude artefacts due to the pressure injection
928 (Supplementary Fig. 2). We found an overall percentage of 37 ± 6.5 % Control
929 neurons and 35.6 ± 9.3 % SLG neurons that did not respond to the stimulation,
930 and were excluded from further analysis.
931
932 **Electron microscopy (EM)**
933 Scanning EM imaging was conducted using collecting secondary electrons on a
934 Gemini SUPRA 40 SEM (Carl Zeiss NTS GmbH, Oberkochen). Before SEM
935 imaging, neuronal cells grown on the different substrates were fixed in 3%
936 Glutaraldehyde in 0.1 M Sodium Cacodylate Buffer (pH 7.4), then dehydrated
937 sequentially in ethanol solutions of 50, 75, 95, 99 and 100% (vol/vol in H_2O, 3
938 minutes each, 4 °C). After overnight drying in the fridge, and before imaging,
939 samples were metalized with a 5 nm thick layer of platinum-iridium alloy using a
940 metal sputter coater (Polaron SC7620). In order to prevent electron induced surface
941 charging, low accelerating voltages (1÷3 keV) were used for cells visualization.
942 SEM images of cells cross sections at membrane-substrate interface were obtained
943 by focused ion beam (FIB) using a LEO-ZEISS Cross-Beam 1540 XB system.
944 Gallium ion beam milling was performed with a current beam of 30 mA while SEM

945 images were collected at 3 kV. Samples were prepared following the same
946 procedure described in the previous paragraph.
947
948 **Substrate characterization**
949 AFM topography data (MFP-3D, Asylum Research, Santa Barbara, California, USA)
950 was acquired in tapping mode, using silicon cantilevers in ambient conditions. The
951 roughness estimates were calculated using the standard deviation of elevation in
952 mapped surface areas with sizes of 10 μm x 10 μm. XPS spectra were recorded in
953 ultra-high vacuum conditions using a monochromatic SPECS XR-50 Mg Kα X-Ray
954 source ($E_{K\alpha}$ = 1253.6 eV) and a hemispherical energy analyser (Phoibos 100/150,
955 Specs, Berlin, Germany). μ-Raman spectra were recorded with an in-house built
956 system using an Ar-ion laser at 514.5 nm and operating with a spectral resolution of
957 0.75 cm^{-1}.
958 Raman measurements in aqueous conditions have been carried out at on the IUVS
959 beamline at Elettra synchrotron radiation facility (Trieste, Italy). A complete
960 description of the experimental apparatus can be found elsewhere
961 [10.1016/j.nima.2012.11.037]. A 532 nm laser source, with a beam power near 5
962 mW, has been employed as excitation source. The scattered radiation was collected
963 in a backscattering geometrical configuration. Slight modifications on the standard
964 backscattering set-up have been introduced to allow measurements in liquid
965 conditions (see Supplementary Methods). A 750 mm focal length Czerny-Turner
966 spectrometer, equipped with an holographic reflection grating of 1800 g/mm and
967 coupled with a Peltier-cooled back-thinned CCD, has been used to get the final
968 Raman spectra.
969

970 **Data Analysis, Statistics and Reproducibility**

971 All values from samples subjected to the same experimental protocols were pooled
972 together and expressed as histograms (mean ± SEM with n = biologically
973 independent experiments, usually number of cells, unless otherwise indicated) or
974 through box plot representation when one or more data set were found to follow a
975 non normal distribution. In box plots, the thick horizontal bar indicates the median
976 value, the boxed area extends from the 25th to 75th percentiles while whiskers from
977 the 5th to the 95th percentiles. The homogeneity of variances was assessed through
978 the Levene's test.

979 Statistically significant difference between two data sets was assessed by Student's
980 t-test for parametric data and by Mann-Whitney for non-parametric ones. Differences
981 between the logarithmic values of the analysed variables were assessed using one-
982 way ANOVA [14] and multiple comparisons were adjusted by Bonferroni correction.
983 Statistical significance was determined at $P < 0.05$, unless otherwise indicated.
984 Significance was graphically indicated as follows: * $P < 0.05$, ** $P < 0.01$, *** $P <$
985 0.001.

986

987 **Mathematical models of single neurons and neuronal networks**

988 Full details on the mathematical models are reported in the Supplementary
989 Information.

990

991 **REFERENCES FOR METHODS**

992 [1] Drieschner, S. et al. Frequency response of electrolyte-gated graphene
993 electrodes and transistors. Journal of Physics D: Applied Physics 50, 095304
994 (2017).

995 [2] Drieschner, S. et al. High surface area graphene foams by chemical vapor
996 deposition. 2D Materials 3, 045013 (2016).
997 [3] Matruglio, A. et al. Contamination-free suspended graphene structures by a
998 Ti-based transfer method Carbon, 103, 305-310 (2016).
999 [4] Lovat, V. et al. Carbon nanotube substrates boost neuronal electrical
1000 signaling. Nano Lett. 5, 1107-1110 (2005).
1001 [5] Cellot, G. et al. Carbon nanotubes might improve neuronal performance by
1002 favouring electrical shortcuts. Nat. Nanotechnol. 4, 126-133 (2009).
1003 [6] Cellot, G. et al, Carbon nanotube scaffolds tune synaptic strength in cultured
1004 neural circuits: novel frontiers in nanomaterial-tissue interactions. J. Neurosci.
1005 31, 12945-12953 (2011).
1006 [7] Pampaloni, NP. et al. Sculpting neurotransmission during synaptic
1007 development by 2D nanostructured interfaces. Nanomedicine. S1549-9634,
1008 30082-5 (2017).
1009 [8] Sontheimer, H. & Ransom, C. Whole-Cell Patch-Clamp Recordings.
1010 Neuromethods 35, 35-67 Humana Press Inc., (2007).
1011 [9] Ruscheweyh, R. & Sandkuhler, J. Lamina-specific membrane and discharge
1012 properties of rat spinal dorsal horn neurones in vitro. J Physiol. 541, 231-244
1013 (2002).
1014 [10] Chang, YM. & Luebke, JI. Electrophysiological diversity of layer 5 pyramidal
1015 cells in the prefrontal cortex of the rhesus monkey: in vitro slice studies. J
1016 Neurophysiol. 98, 2622-32. (2007)
1017 [11] Renganathan, M., Cummins, TR. & Waxman, SG. Contribution of Na(v)1.8
1018 sodium channels to action potential electrogenesis in DRG neurons. J
1019 Neurophysiol. 86, 629-40 (2001).

[12] Furlan, F. et al. ERG conductance expression modulates the excitability of ventral horn GABAergic interneurons that control rhythmic oscillations in the developing mouse spinal cord. J. Neurosci. 27, 919-928 (2007).

[13] Usmani S, et al. 3D meshes of carbon nanotubes guide functional reconnection of segregated spinal explants. Sci Adv. e1600087 (2016).

[14] Wilcox RR & Rousselet GA. A Guide to Robust Statistical Methods in Neuroscience. Curr Protoc Neurosci. 82, 8.42.1-8.42.30 (2018).

Additional information

Supplementary information are available in the online version of the paper.

Correspondence and requests to Denis Scaini dscaini@sissa.it; Josè Antonio Garrido joseantonio.garrido@icn2.cat; Laura Ballerini laura.ballerini@sissa.it

Data availability

The data that support the plots within this paper and other findings of this study are available from the corresponding authors upon reasonable request. The mathematical model is available online at ModelDB (https://senselab.med.yale.edu/ModelDB/).

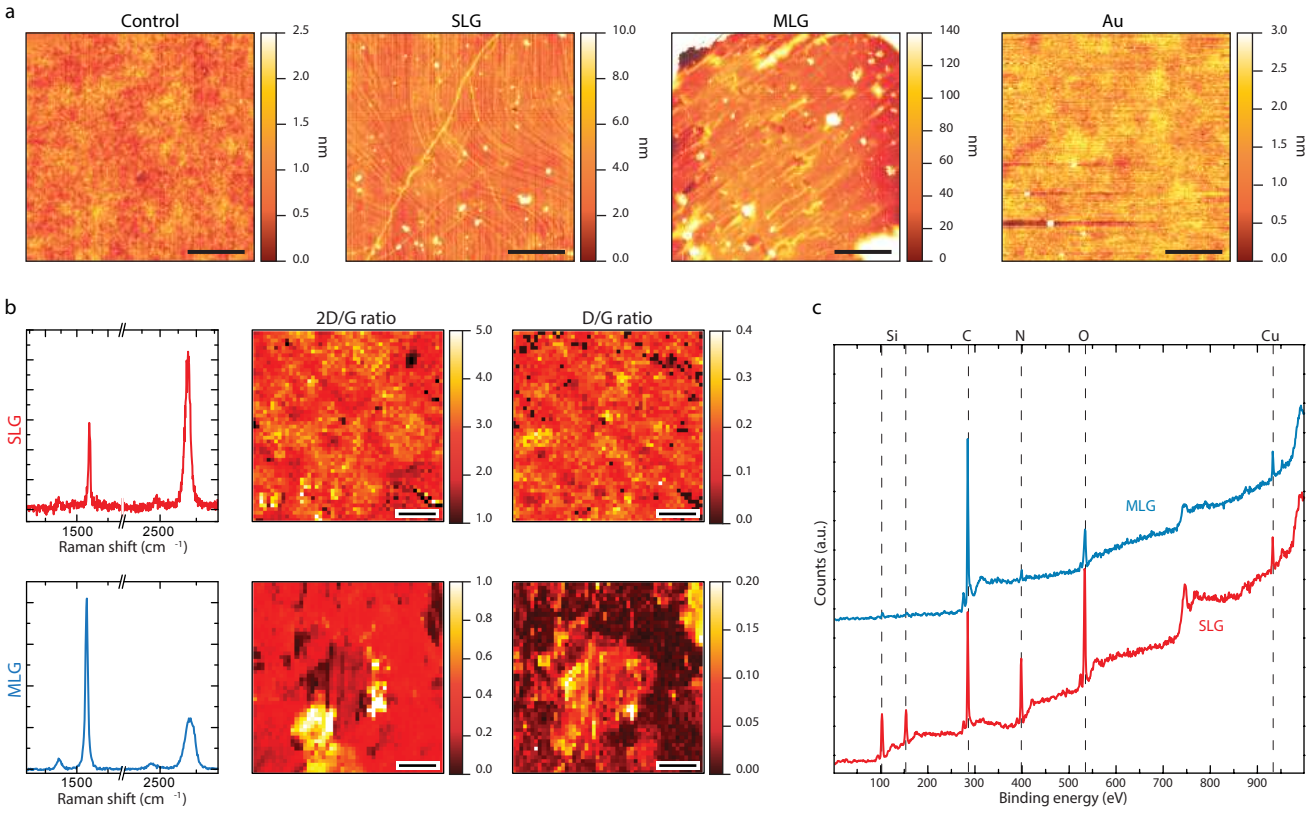
a
Control
SLG
MLG
Au
nm
b
2D/G ratio
D/G ratio
SLG
MLG
1500
2500
Raman shift (cm -1)
c
Si
C
N
O
Cu
MLG
SLG
Counts (a.u.)
Binding energy (eV)

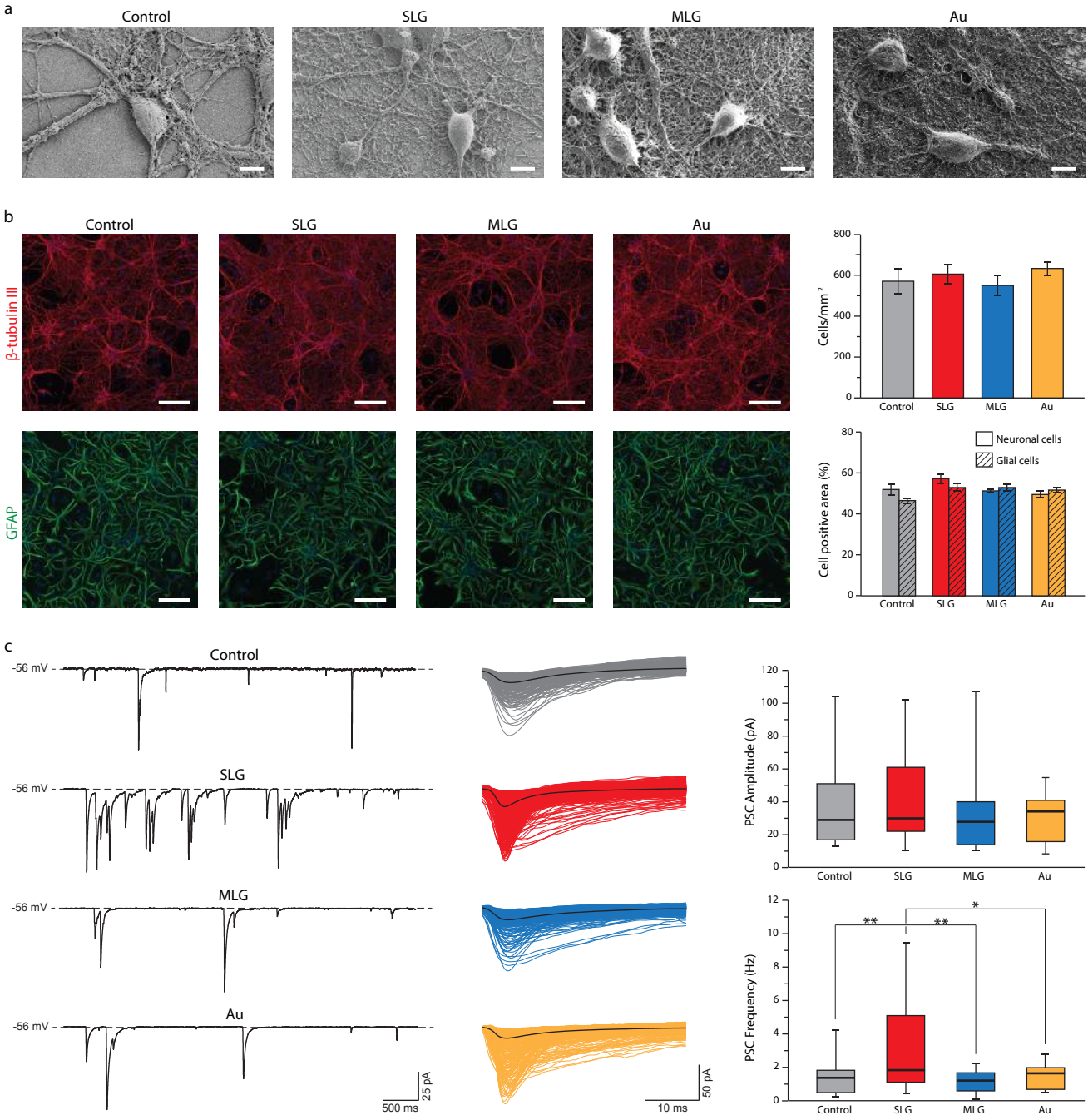
a
Control
SLG
MLG
Au
b
Control
SLG
MLG
Au
β-tubulin III
GFAP
Cells/mm 2
800
600
400
200
0
Control
SLG
MLG
Au
Neuronal cells
Glial cells
Cell positive area (%)
80
60
40
20
0
c
Control
SLG
MLG
Au
-56 mV
25 pA
500 ms
50 pA
10 ms
PSC Amplitude (pA)
120
100
80
60
40
20
0
PSC Frequency (Hz)
12
10
8
6
4
2
0
**
**
*

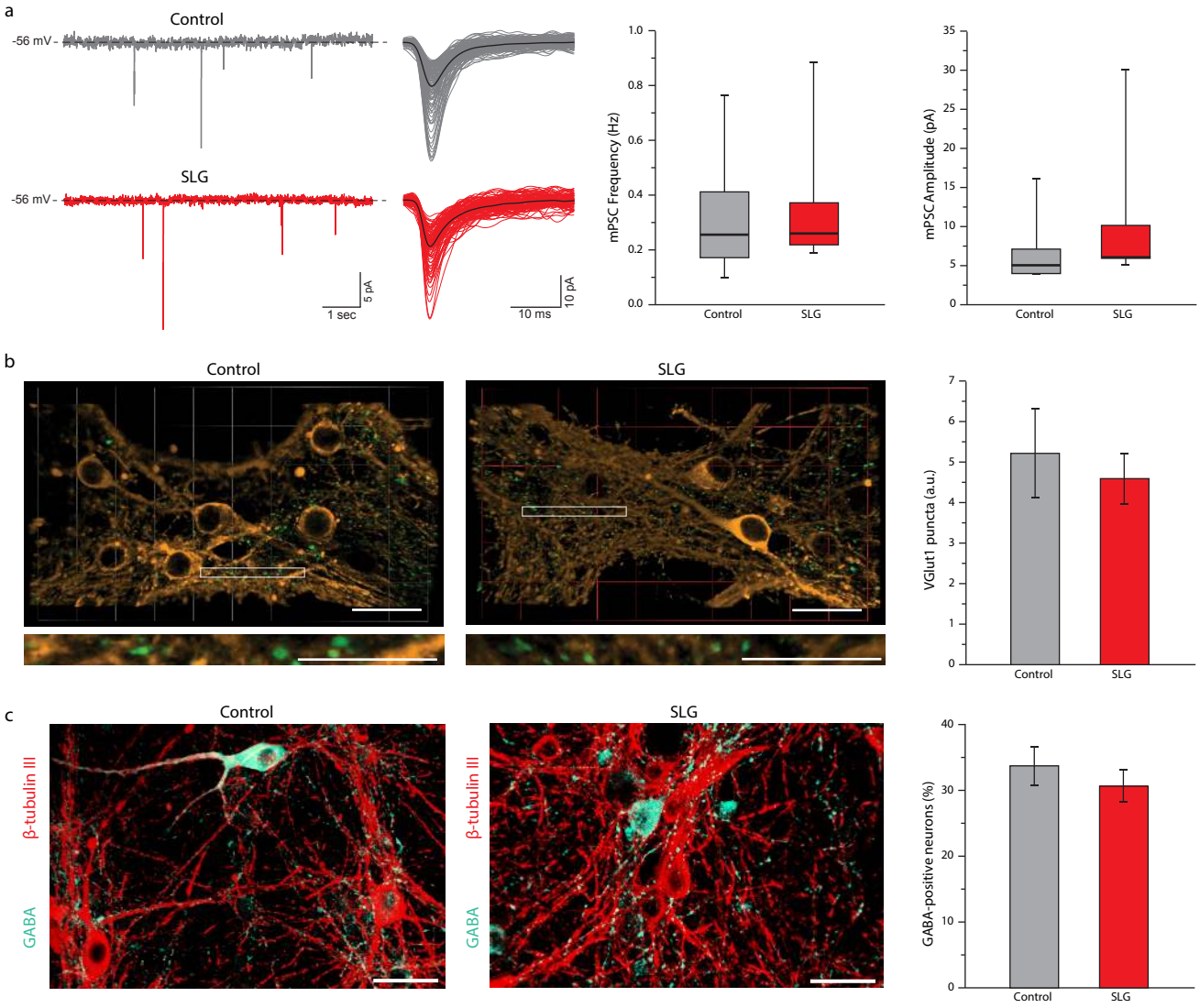
a
Control
-56 mV
SLG
-56 mV
1 sec
5 pA
10 ms
10 pA
mPSC Frequency (Hz)
1.0
0.8
0.6
0.4
0.2
0.0
Control
SLG
mPSC Amplitude (pA)
35
30
25
20
15
10
5
0
Control
SLG
b
Control
SLG
VGlut1 puncta (a.u.)
7
6
5
4
3
2
1
0
Control
SLG
c
Control
SLG
β-tubulin III
GABA
β-tubulin III
GABA
GABA-positive neurons (%)
40
30
20
10
0
Control
SLG

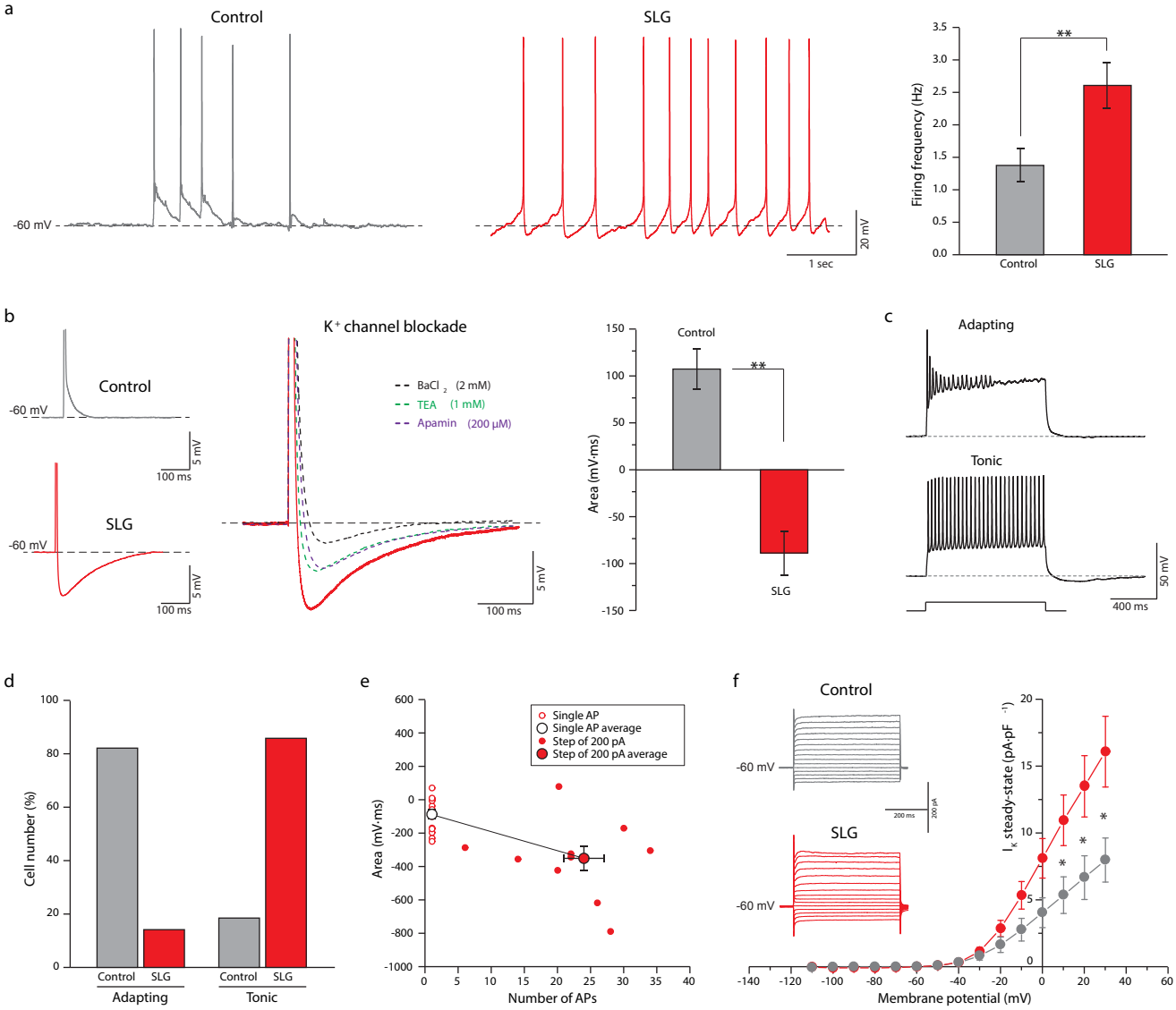
a
Control
SLG
-60 mV
20 mV
1 sec
Firing frequency (Hz)
Control
SLG
b
Control
SLG
-60 mV
5 mV
100 ms
K+ channel blockade
BaCl2 (2 mM)
TEA (1 mM)
Apamin (200 μM)
Area (mV·ms)
c
Adapting
Tonic
50 mV
400 ms
d
Cell number (%)
Control
SLG
Adapting
Tonic
e
Single AP
Single AP average
Step of 200 pA
Step of 200 pA average
Area (mV·ms)
Number of APs
f
Control
SLG
-60 mV
200 ms
200 pA
Membrane potential (mV)

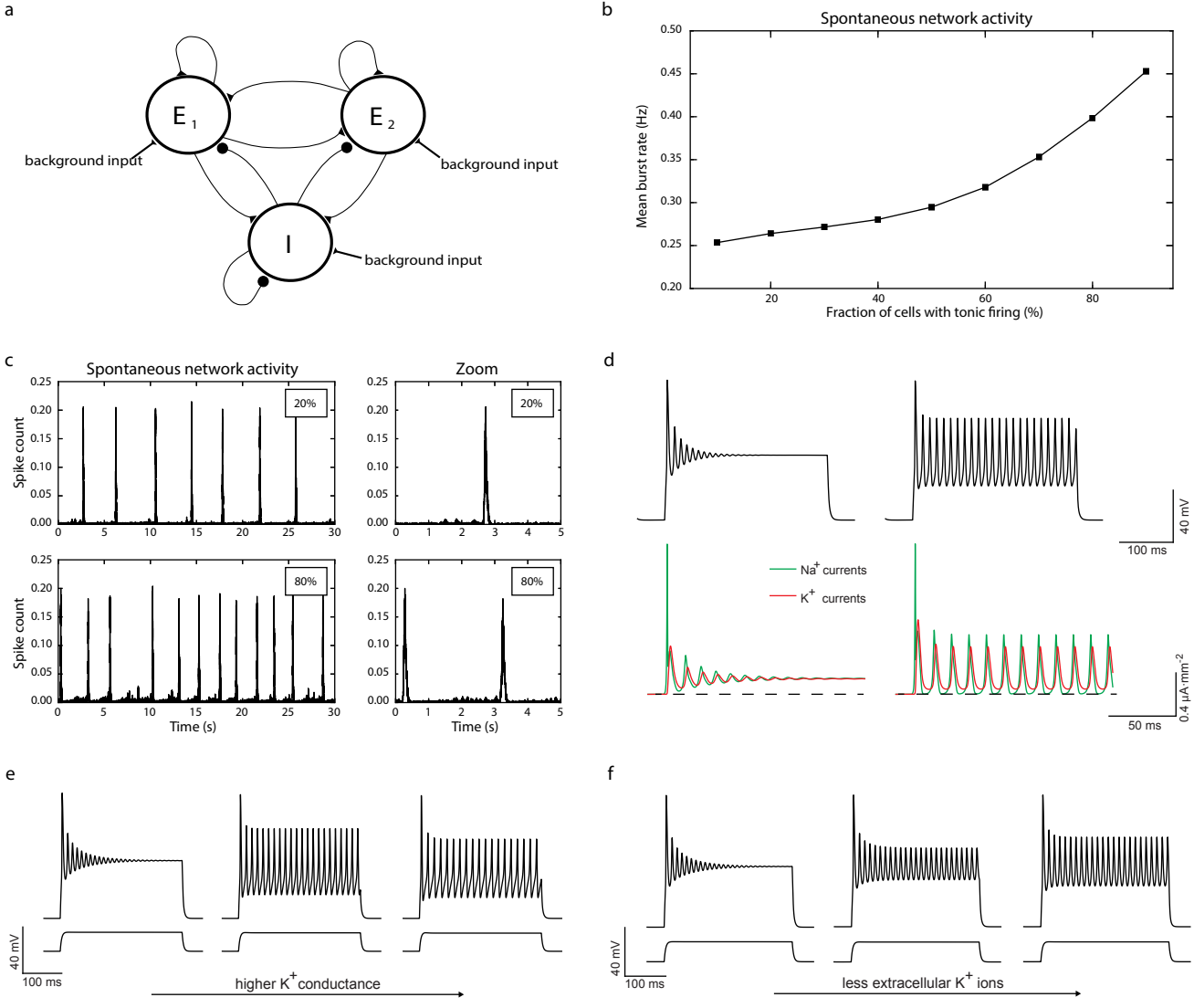
a
E 1
E 2
I
background input
background input
background input
b
Spontaneous network activity
Mean burst rate (Hz)
Fraction of cells with tonic firing (%)
c
Spontaneous network activity
Zoom
Spike count
Time (s)
20%
80%
d
Na+ currents
K+ currents
40 mV
100 ms
0.4 μA·mm-2
50 ms
e
40 mV
100 ms
higher K+ conductance
f
40 mV
100 ms
less extracellular K+ ions

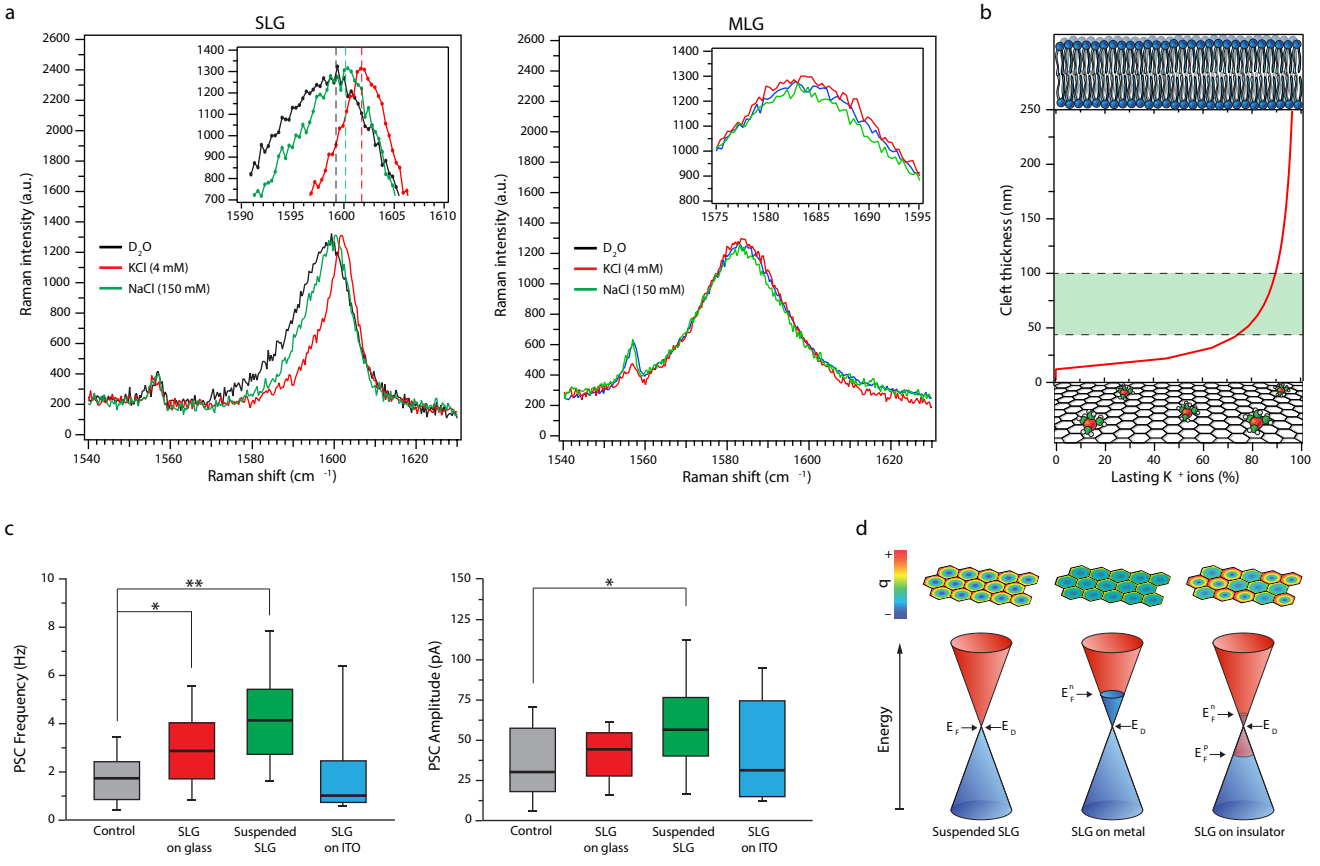
a
SLG
MLG
Raman intensity (a.u.)
Raman shift (cm -1)
D2O
KCl (4 mM)
NaCl (150 mM)
b
Cleft thickness (nm)
Lasting K + ions (%)
c
PSC Frequency (Hz)
PSC Amplitude (pA)
Control
SLG on glass
Suspended SLG
SLG on ITO
d
q
Energy
Suspended SLG
SLG on metal
SLG on insulator